

Non-relativistic linear Edelstein effect in non-collinear EuIn_2As_2

Nayra A. Álvarez Pari,¹ Rodrigo Jaeschke-Ubiergo,¹ Atasi Chakraborty,¹ Libor Šmejkal,^{2,3,1,4} and Jairo Sinova^{1,5}

¹*Institut für Physik, Johannes Gutenberg Universität, D-55099 Mainz, Germany*

²*Max Planck Institute for the Physics of Complex Systems, Nöthnitzer Str. 38, 01187 Dresden, Germany*

³*Max Planck Institute for Chemical Physics of Solids, Nöthnitzer Str. 40, 01187 Dresden, Germany*

⁴*Institute of Physics, Academy of Sciences of the Czech Republic, Cukrovarnická 10, 162 00 Praha 6, Czech Republic*

⁵*Department of Physics, Texas A & M University, College Station, Texas 77843-4242, USA*

(Dated: December 17, 2024)

Motivated by the ongoing interest in understanding the actual magnetic ground state of the promising axion insulator candidate EuIn_2As_2 , we present here a spin symmetry analysis and *ab initio* calculations, aiming to identify specific exchange-dominated physics that could offer insights into the current debate. We investigate two non-collinear coplanar magnetic orders reported in this compound: the *helical* and *broken helical* phases. Our symmetry analysis shows that magnetic-exchange alone results in the formation of an out-of-plane odd-wave order in momentum space with a single un-polarized nodal plane in both phases. Additionally, we identified an in-plane g-wave order that emerges exclusively in the *broken helical* phase, providing a distinguishing feature for this phase. Furthermore, we report a non-relativistic Edelstein effect with a distinct out-of-plane polarized spin density that dominates over spin-orbit coupling effects. Our *ab initio* calculations reveal a significant contrast in the magnitude of this effect between both phases, which could serve as a means to identify the magnetic transition and distinguish them from other magnetic ground states proposed for this compound.

I. INTRODUCTION

Understanding the intricate interplay between magnetic and topological properties of quantum materials is a fundamental challenge in condensed matter physics. The mutual influence is particularly evident in materials where electronic and magnetic degrees of freedom are coupled, as magnetic order can alter the energy dispersion and lead to unique topological features. In this context, the Eu-based 122 compounds have attracted considerable interest due to their intrinsic spin-orbit coupling arising from their strongly localized *f*-orbitals, which can lead to distinctive electronic, magnetic, and topological properties in the band structures. The realization of various quantum phases within this family, including exotic topological surface states [1–4], colossal magnetoresistance [5–7], and the axion electrodynamics [8, 9], makes them a promising magnetic topological platform for future spintronic applications.

The rare-earth compound EuIn_2As_2 has caught the spotlight within the 122 family after first-principle studies have proposed it as a candidate axion insulator, assuming a simple antiferromagnetic collinear order [8, 10]. However, this initial claim was quickly contested by experimental studies proposing various magnetic orders, from commensurate [11–13] to incommensurate non-collinear magnetic order [14, 15]. The magnetic structures reported by Riberolles et al. and Soh et al. [11, 12] suggest coplanar non-collinear magnetic structures: the *helical* and *broken-helical* phases. The *helical* phase, which emerges at $T_{N_1} = 17.6(2)$ K, is characterized by connecting adjacent magnetic layers by 60° rotation along \hat{z} , as shown in Fig.2(a). At lower temperatures $T_{N_2} = 16.2(1)$ K, the *broken-helical* phase emerges, with a magnetic configuration involving two symmetry-independent Eu magnetic sub-lattices, highlighted in red

and blue in Fig.2(b). Additionally, recent first-principle studies have revealed non-relativistic spin splittings in the collinear magnetic configuration [16]. Therefore, studying this compound employing spin symmetries [17, 18] could offer valuable information on the effects of magnetic exchange on the electronic band structure.

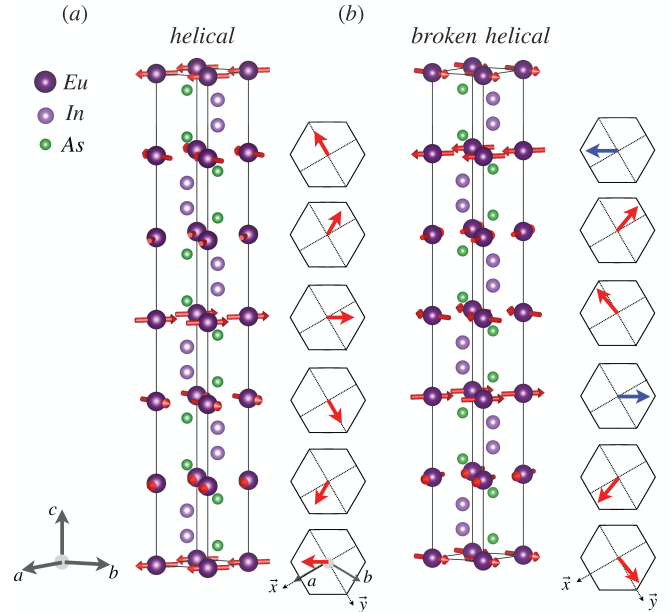


FIG. 2. Non-collinear coplanar magnetic textures of EuIn_2As_2 . (a) The *helical* phase, with neighboring magnetic layers connected by 60° rotation along \hat{z} . (b) The *broken-helical* phase, with two symmetry-independent Eu magnetic sub-lattices. The red-red sublattices are connected by 80° and the red-blue spin sublattices by 130° . For both phases, a tripling of the unit cell along $\mathbf{c} = c \hat{\mathbf{z}}$ is assumed [11, 12].

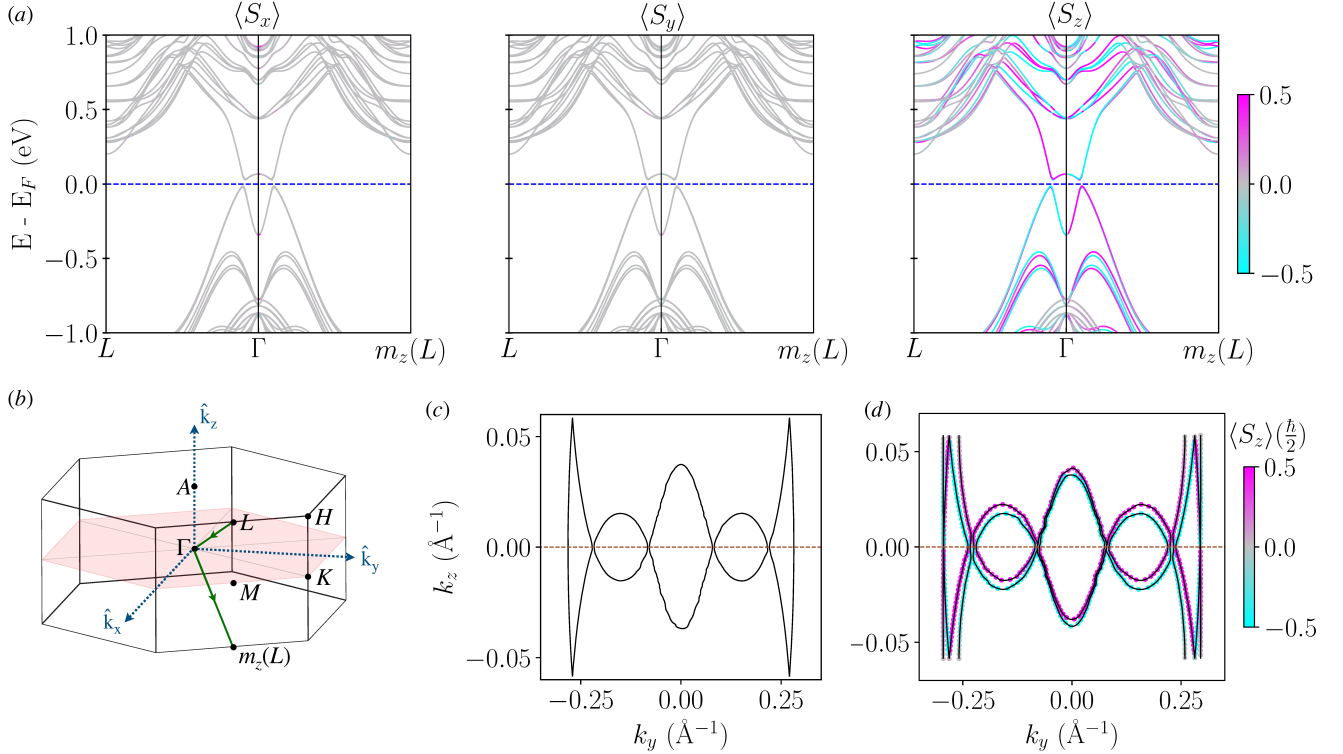


FIG. 1. Electronic band structures and Fermi surfaces without SOC for the non-collinear *helical* EuIn_2As_2 phase. (a) Energy bands along the momentum space path $L - \Gamma - m_z(L)$. Spin un-polarized bands for S_x and S_y spin projections, and spin-polarized bands with visible spin splittings for the S_z spin component. (b) The hexagonal first Brillouin zone (1BZ) and the single nodal plane at $k_z = 0$ (red) allowed for the S_z spin component. (c) Fermi surfaces in the momentum space $k_x = 0$ plane for the non-magnetic crystal and (d) for the *helical* order for an energy $E = -0.60\text{eV}$. The non-magnetic unit cell has been tripled along z -axis for comparison reasons.

Here, we systematically analyze the spin symmetries of individual *helical* and *broken-helical* phases reported for EuIn_2As_2 . Our study reveals several key similarities and notable contrasting characteristics between the two phases. We identify an out-of-plane odd-wave order in momentum space in both non-collinear phases. This odd-parity spin splitting reaches up to 100 meV in the *helical* phase and 20 meV in the *broken helical* phase. Additionally, we find that in the *broken-helical* phase, the breaking of certain symmetries induces an in-plane g-wave order, which can be probed through spectroscopic techniques. Finally, we validate the odd-parity wave nature of these phases by calculating a non-equilibrium spin-polarization generated by an applied electric field, known as the Edelstein effect. We report a unique out-of-plane non-relativistic linear Edelstein response that dominates over the spin-orbit coupling effects. This feature can also distinguish from other proposed commensurate amplitude modulated phases [13], which would not have this effect.

This article is organized as follows. In sections II and III, we characterize the non-relativistic spin-momentum locking for the *helical* and *broken helical* phases, employing a spin symmetry analysis and *ab initio* calculations. In Section IV, we introduce the linear Edelstein effect in non-centrosymmetric systems, discuss the symmetry-imposed spin density, and validate the findings with computed Edelstein effect for both phases. Finally, in the Section V we present our conclusions.

II. SPIN SYMMETRY ANALYSIS OF THE HELICAL PHASE

In the non-relativistic regime, where spin and crystal lattice are decoupled, Spin space groups (SSGs) provide a proper description of the magnetic part of the electronic spectra. These symmetry transformations come as pairs of operators that act on the spin and real space separately. The spin-space group can be decomposed as a direct product between the spin-only group and the non-trivial spin-space group, $\mathbf{r}_s \times \mathcal{G}_s$. This factorization is done in such a way that the \mathcal{G}_s contains only unitary symmetries. The spin-only group for coplanar non-collinear magnets is $\mathbf{r}_s = \{[E||E], [C_{2\perp}\mathcal{T}||\mathcal{T}]\}$, where $C_{2\perp}$ represents a 180° spin-space rotation around the axis perpendicular to the coplanar magnetic moments, E represents the identity operator, and \mathcal{T} the time reversal symmetry.

To evaluate the symmetry constraints imposed on the electronic band structure around Γ , one can ignore the translations and therefore focus on the product $\mathbf{r}_s \times \mathbf{R}_s$, with \mathbf{R}_s the non-trivial spin point group. The spin point group for the *helical* phase is given by

$$\mathbf{R}_s^H = \left([3||3m] + [3\mathbf{2} - \mathbf{3}||\mathcal{P} \cdot 3m] \right) \times \left\{ [E||E], [C_{6z}||C_{6z}] \right\}, \quad (1)$$

with $\mathbf{3\mathbf{2}} = \{E, C_{3z}, C_{-3z}, C_{2v}, C_{2v'}, C_{2v''}\}$, $\mathbf{3} = \{E, C_{3z}, C_{-3z}\}$ point groups acting only in the spin-space,

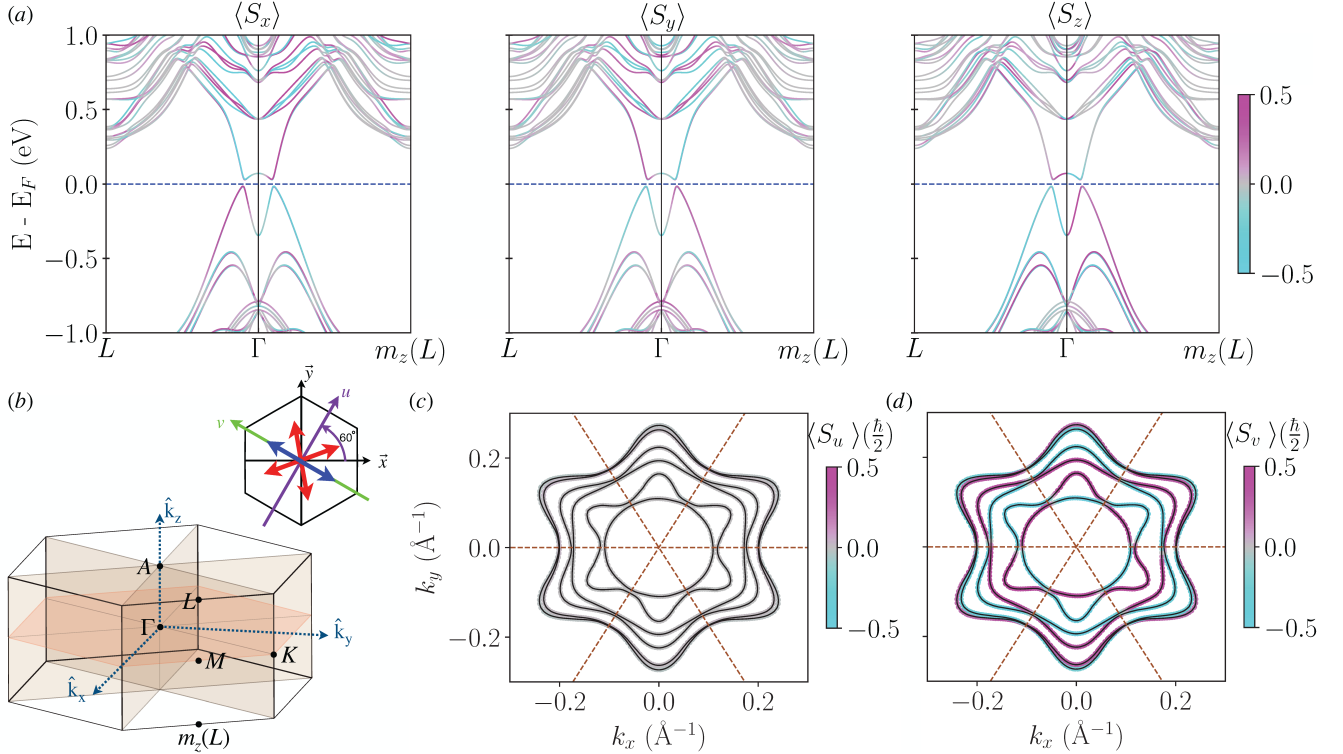


FIG. 3. Electronic band structure and Fermi surfaces of odd-wave and g-wave spin textures without SOC in the non-collinear *broken-helical* EuIn_2As_2 order. (a) Spin-polarized energy bands along x , y , and z directions, plotted along the momentum path $L - \Gamma - m_z(L)$. (b) The hexagonal BZ and the four nodal planes associated with the g-wave order, each separating regions of opposite spin polarization. The inset in the top right highlights the orthogonal spin axes u (violet), and v (green), which are chosen to visualize the in-plane g-wave spin texture. The red and blue arrows represent the directions of the Eu magnetic moments. (c) Spin-polarized Fermi surfaces in the momentum space $k_z = 0.2c$ plane for an energy $E = 0.60$ eV, along the u and v spin directions. A spin un-polarized Fermi surface is observed for the S_u spin component, while (d) a purely g-wave spin texture is seen for the S_v spin component. The mustard-dotted lines indicate the nodal planes.

and $3m = \{E, C_{3z}, C_{-3z}m_u, m_{u'}, m_{u''}\}$ operating in the real-space. The full non-trivial spin space group \mathcal{G}_s^H , the generators, and the corresponding axes $\{v, v', v''\}$ are specified in App. B.

We see that \mathbf{R}_s^H preserves the symmetries $[C_{3z}||E]$ and $[C_{-3z}||E]$, which act exclusively within the spin-space, resulting into an out-of-plane spin polarization in the band structure, i.e., $\langle S_x \rangle = 0$ and $\langle S_y \rangle = 0$. Additionally, the spin point group has $[C_{2z}||C_{2z}]$, which in combination with the coplanar spin-only group $[C_{2z}\mathcal{T}||\mathcal{T}]$ symmetry, results in $S_z(k_x, k_y, k_z) = -S_z(k_x, k_y, -k_z)$, resulting in a single spin-unpolarized plane at $k_z = 0$. This antisymmetric spin texture, characterized by an odd number of nodal planes in momentum space, can also be referred to as odd-wave magnetism.

We next perform spin-polarized density functional theory (DFT) band structure calculations to confirm the findings of the symmetry analysis. All the methodology used here and in the following sections is presented in App. A. We select the $L - \Gamma - m_z(L)$ path, which intersects the nodal plane $k_z = 0$, as illustrated in Fig. 1(b). The energy bands without SOC, shown for each spin projection in Fig. 1(a), reveal spin-polarized bands exclusively for the S_z spin projection, with spin splittings reaching up to 100 meV. This antisymmetric spin polarization can be visualized in the Fermi surface calculations along the $k_x = 0$ plane, shown

in Fig. 1(d). A comparison between the Fermi surface of the non-magnetic order in Fig 1(c) and the one under helical order reveals that the spin splittings are of non-relativistic origin, arising primarily due to magnetic exchange between local and itinerant electrons.

We point out that the odd-wave magnetism we observe, featuring one spin-degenerate nodal plane, differs from the recently reported p-wave ordering in coplanar non-centrosymmetric magnetic crystal structures [19]. The key distinction is that p-wave magnetism requires materials with $\mathcal{T}\tau$ symmetry, which manifests as a linear energy dispersion near Γ . In our case, $\mathcal{T}\tau$ is broken, but the combination $[\mathcal{T}||C_{2z}\mathcal{T}|\tau]$ is preserved, resulting in an odd order parameter and a quadratic dispersion near Γ , as shown in the band structures in Fig. 1(a).

III. SPIN SYMMETRY ANALYSIS OF THE BROKEN-HELICAL PHASE

This more complex magnetic configuration, results in a smaller non-trivial spin space group, see App. B. Excluding the translations, the non-trivial spin point group can be written as

$$\mathbf{R}_s^B = \left([E||3m] + [C_{2z}||6mm - 3m] \right) \times \left\{ [E||E], [C_{2v}||P] \right\}, \quad (2)$$

with $6mm = \{E, C_{3z}, C_{-3z}, C_{6z}, C_{-6z}, C_{2z}, m_u, m_{u'}, m_{u''}, m_v, m_{v'}, m_{v''}\}$.

Focusing on \mathbf{R}_s^B , we can identify a similarity between the first term in parenthesis and the spin point group of the collinear g-wave altermagnetic phase of EuIn_2As_2 , see App. C. The spin rotation C_{2z} has an axis orthogonal to the in-plane spins, analogous to the C_2 spin rotation in an altermagnetic point group [20]. This suggests that both the S_x and S_y spin components will exhibit a g -wave order. The second term in brackets connects the spin textures in S_x and S_y , with the symmetry $[C_{2v}||P]$ keeping invariant a g -wave order for S_v while completely suppressing it for S_u . As a result, the uv -axes (see top-right inset in Fig. 3(b)) exhibits the in-plane g -wave order. Regardless of the choice of the spin axis, the four spin-degenerate nodal planes of the g -wave order are protected by the following transposing mirror symmetries: $[C_{2z}||m_v]$, $[C_{2z}||m_{v'}]$, $[C_{2z}||m_{v''}]$, and $[C_{2z}||m_z]$. The axes v' , and v'' , are defined in App. B. Finally, similar to the *helical* order, the symmetry $[C_{2z}||C_{2z}]$ is preserved, indicating that an odd-wave order is expected for the spin component S_z , with a nodal plane at $k_z = 0$.

In Fig. 3, we present the DFT calculations for the *broken-helical* order. The 1BZ with four nodal planes of the g -wave order are illustrated in Fig. 3(b). To visualize the alternating spin polarization in the energy bands, we select the path $L - \Gamma - m_z(L)$, which intersects one of the nodal planes. In Fig. 3(a), we see the spin-polarized bands setting the spin-axis along the conventional xyz axis. We observe spin splitting reaching up to 60 meV. We also see antisymmetric spin splittings for the S_z spin component, but significantly reduced, with values up to 20 meV. Finally, setting the spin-axis along uv , the Fermi surfaces in Fig 3(c,d) display un-polarized bands for S_u and a g -wave order for S_v , which agree with our symmetry analysis.

IV. NON-RELATIVISTIC LINEAR EDELSTEIN EFFECT

The Edelstein effect refers to the generation of a non-equilibrium spin density by an applied electric field in non-centrosymmetric systems. Traditionally, this effect has been associated with spin-orbit coupling [21–23]. However, recent studies have demonstrated that a non-relativistic Edelstein effect can also occur in non-collinear non-centrosymmetric compounds with an antisymmetric spin texture or coplanar p-wave magnets [24, 25].

The non-equilibrium spin density can be calculated using the Kubo linear response formalism, [21, 26]. i.e., $\delta s_i = \chi_{ij} E_j$ with χ_{ij} as the response tensor and E_j the electric field. The response tensor can be decomposed into two components, the \mathcal{T} -even (intraband) and \mathcal{T} -odd (interband) contributions [21, 27]. The intraband term is given by

		No SOC	SOC
Helical	χ^{even}	$\begin{pmatrix} 0 & 0 & 0 \\ 0 & 0 & 0 \\ 0 & 0 & \chi_c \end{pmatrix}$	$\begin{pmatrix} \chi_a & \chi_a/2 & 0 \\ \chi_a/2 & \chi_a & 0 \\ 0 & 0 & \chi_c \end{pmatrix}$
	χ^{odd}	$\begin{pmatrix} 0 & 0 & 0 \\ 0 & 0 & 0 \\ 0 & 0 & 0 \end{pmatrix}$	$\begin{pmatrix} 0 & \chi_b & 0 \\ -\chi_b & 0 & 0 \\ 0 & 0 & 0 \end{pmatrix}$
Broken Helical	χ^{even}	$\begin{pmatrix} 0 & 0 & 0 \\ 0 & 0 & 0 \\ 0 & 0 & \tilde{\chi}_c \end{pmatrix}$	$\begin{pmatrix} \tilde{\chi}_a & \tilde{\chi}_b & 0 \\ \tilde{\chi}_b & \tilde{\chi}_a & 0 \\ 0 & 0 & \tilde{\chi}_c \end{pmatrix}$
	χ^{odd}	$\begin{pmatrix} 0 & 0 & 0 \\ 0 & 0 & 0 \\ 0 & 0 & 0 \end{pmatrix}$	$\begin{pmatrix} \tilde{\chi}_a & \tilde{\chi}_b & 0 \\ -\tilde{\chi}_b & -\tilde{\chi}_a & 0 \\ 0 & 0 & 0 \end{pmatrix}$

TABLE I. Shape of the \mathcal{T} -even and \mathcal{T} -odd response tensor χ for the helical and broken-helical orders expressed as a function of the lattice vectors, $\mathbf{a} = a\hat{\mathbf{x}}$, $\mathbf{b} = -a\frac{\sqrt{3}}{2}\hat{\mathbf{x}} + \frac{a}{2}\hat{\mathbf{y}}$, and $\mathbf{c} = c\hat{\mathbf{z}}$. In the non-relativistic case, the spin-point group generators are applied while for the relativistic case, magnetic-point group generators are employed

$$\chi_{ij}^{even} = \frac{e\hbar}{2\Gamma} \int \frac{d^3\vec{k}}{(2\pi)^3} \sum_n \text{Re}[(\hat{s}_i)_{nn}(\hat{v}_j)_{nn}] \times \delta(E_{\vec{k}n} - E_F), \quad (3)$$

with e as the electric charge, $E_{\vec{k}n}$ the n -th energy band for a given \vec{k} wave vector, E_F the Fermi energy, \hat{s}_i the spin operator, \hat{v}_j the velocity operator, and Γ the spectral broadening due to disorder.

The interband term is given by

$$\chi_{ij}^{odd} = 2e\hbar \int \frac{d^3\vec{k}}{(2\pi)^3} \sum_{n \neq m} (f_{\vec{k}n} - f_{\vec{k}m}) \text{Im}[(s_i)_{nm}(v_j)_{mn}] \times \frac{(E_{\vec{k}n} - E_{\vec{k}m})^2 - \Gamma^2}{[(E_{\vec{k}n} - E_{\vec{k}m}) + \Gamma^2]^2}, \quad (4)$$

with $f_{\vec{k}n}$ as the Fermi distribution function, and n and m correspond to different bands.

As previously reported, the helical and broken-helical orders of EuIn_2As_2 exhibit a non-relativistic antisymmetric spin texture for the S_z spin component while simultaneously breaking \mathcal{P} symmetry. As a result, a non-relativistic Edelstein effect is expected for both configurations. To begin, we analyze the symmetry imposed shape of the response tensor χ_{ij} under the spin-symmetry generators (see Table I). In the absence of spin-orbit coupling, only the intraband contribution along the lattice vector \mathbf{c} , χ_{cc}^{even} , is allowed for both non-collinear orders. This suggests that an electric field applied along the z direction can generate a non-equilibrium out-of-plane spin population. When spin-orbit coupling is introduced, additional in-plane intraband components are allowed, and the interband contribution becomes possible.

From the symmetry analysis, we find that only the out-of-plane intraband contribution is directly linked to the

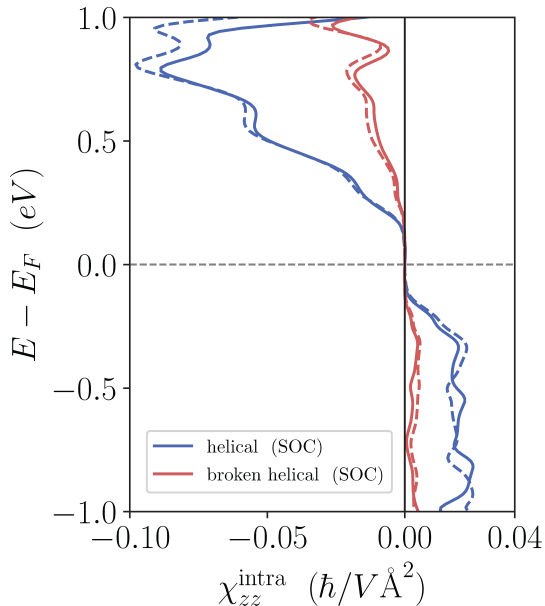


FIG. 4. Computed intraband out-of-plane response tensor χ_{zz}^{even} . Calculations with (solid line) and without (dashed line) spin-orbit coupling of both the *helical* and *broken-helical* phases considering a disorder $\Gamma = 0.01$ eV.

non-relativistic spin momentum locking. We report this contribution with and without SOC in Fig. 4. The *helical* phase exhibits spin density δs_z values larger than those in the *broken helical* phase, with $\chi_{zz}^{helical}/\chi_{zz}^{broken} \approx 5$ within $E = E_F \pm 0.3$ eV, which is consistent with the fact that the odd-parity spin splittings in both phases also differ by the same factor. Introducing spin-orbit coupling does not significantly affect the out-of-plane spin density values, but it originates in-plane terms with a little effect compared to the dominant out-of-plane response, see App. D. The significant difference in the out-of-plane polarized spin density values between both phases could serve as a signature for detecting the magnetic transition via transport measurements, in contrast to other transport quantities, such as the longitudinal conductivity, which also shows differences between both phases but to a lesser extent, see App. E. While the spin density vanishes at the Fermi level, being a semiconductor material, doping can shift the Fermi level [28] and induce sizeable values of the Edelstein response.

A final important point with regards to the measurement of the Edelstein effect, is that its presence – or lack of presence – will also serve to validate or discard the proposed amplitude modulated phases in Ref. [13], since both their A_1 (P symmetric) and A_2 (PT symmetric) phases would not have an Edelstein effect.

V. CONCLUSION

We have studied two non-collinear coplanar phases of EuIn_2As_2 , the *helical* and *broken-helical* phases, which were previously identified through neutron and x-ray scattering. For each magnetic phase, we have performed a spin

symmetry analysis and confirmed our findings with *ab initio* calculations, which showed good agreement between the two approaches.

Our symmetry analysis predicts an out-of-plane odd-wave magnetism with a single nodal plane in both phases, implying the presence of odd-parity spin splittings in each. Additionally, a current-induced spin density, known as the Edelstein effect, can occur due to the antisymmetric spin textures in momentum space, even in the absence of spin-orbit coupling. Remarkably, our calculations reveal a distinctive out-of-plane polarized spin density, showing a larger effect in the *helical* phase than in the *broken helical* phase. Such contrasting differences in this anisotropic response could serve as an alternative indicator of the magnetic transition between the two phases. It may also help differentiate them between the magnetic ground states recently proposed by Donoway et al. [13] involving amplitude modulation (phase A_1 and A_2), which do not exhibit a linear Edelstein response, even in the presence of spin-orbit coupling.

Furthermore, we identified a key distinguishing feature between both phases: the appearance of an in-plane g-wave magnetism exclusively in the *broken helical* phase. This distinctive characteristic offers another signature to distinguish between the phases using spectroscopic techniques, and the possibility to explore the interplay between the g-wave order parameter and the topology of the axion insulator phase in this material.

Acknowledgments— This work is supported by the Deutsche Forschungsgemeinschaft (DFG, German Research Foundation) — TRR 288 – 422213477 (project B05 and A09). AC acknowledges financial support from Alexander von Humboldt foundation. LS acknowledges support by Grant Agency of the Czech Republic grant no. 19-28375X. We acknowledge fruitful discussions with Rafael González-Hernández, Veronika Sunko and Anna Birk Hellenes.

Appendix A: Computational Methods

The electronic band structures were performed within DFT, using the Vienna ab-initio Simulation Package (VASP) [29, 30], and the Perdew-Burke-Ernzerhof (PBE) exchange-correlation functional was applied as the generalized gradient approximation (GGA) [31]. To capture the non-relativistic effects, both the spin-orbit coupling and the symmetrization were switched off. A Hubbard U of 5 eV was included to account for the localized nature of the Eu 4f orbitals. The Brillouin zone was sampled with a Γ -centered k-point mesh of $13 \times 13 \times 3$, along with a Gaussian smearing of 0.05 eV, a kinetic energy cutoff of 250 eV, and a convergence criterion of 10^{-6} eV were used. The self-consistent calculations were carried out using constraints in the magnetic moment's directions as reported in MAGNDATA [32, 33]. Applying constraints introduces a penalty energy, which indicates the deviation from the desired magnetic moments [34]. The penalty energies achieved for both the *helical* and *broken-helical* orders were 10^{-8} eV.

The spin-polarized energy bands and Fermi surface

plots were generated using PyProcar [35]. Additionally, we employed the *spinspg* package [36] to determine the corresponding spin symmetries. For further data analysis and post-processing, a tight-binding Hamiltonian was generated within the projected Wannier functions for Eu d, f , In s, p , and As p orbitals using the Wannier90 package [37]. The charge-induced spin density was then calculated using the Wannierberri package [38] with a finite momentum k -mesh of $162 \times 162 \times 12$.

Appendix B: Spin space groups

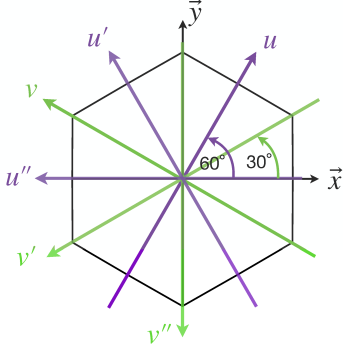


FIG. 5. Six in-plane axes, $\{u, u', u''\}$ (green), and $\{v, v', v''\}$ (violet), where each pair $\{u, v\}$, $\{u', v'\}$, and $\{u'', v''\}$ consists of orthogonal axes.

The non trivial spin space group of the *helical* order can be written as

$$\mathcal{G}_s^H = \left([E||3m] + [C_{2v}||\mathcal{P} \cdot 3m] + [C_{6z}||6mm - 3m|\tau] + [C_{2u''}||\mathcal{P} \cdot (6mm - 3m)|\tau] + [C_{3z}||3m|2\tau] + [C_{2v'}||\mathcal{P} \cdot 3m|2\tau] + [C_{2z}||6mm - 3m|3\tau] + [C_{2u}||\mathcal{P} \cdot (6mm - 3m)|3\tau] + [C_{-3z}||3m|4\tau] + [C_{2v''}||\mathcal{P} \cdot 3m|4\tau] + [C_{-6z}||6mm - 3m|5\tau] + [C_{2u'}||\mathcal{P} \cdot (6mm - 3m)|5\tau] \right),$$

with $C_{2\{u, u', u''\}}$ and $C_{2\{v, v', v''\}}$ representing C_2 -fold rotations along in-plane axes shown in Fig. 5, and the translation $\tau = (0, 0, \frac{1}{6}c)$. The generators of the *helical* spin space group are $[C_{6z}||C_{6z}|\tau]$, $[C_{6z}||m_v|\tau]$, $[C_{2v}||\mathcal{P}]$, and $[C_{2z}\mathcal{T}||\mathcal{T}]$. The last antiunitary generator arises from the spin only group of a coplanar system.

The non-trivial spin-space group of the *broken-helical* order can be written as

$$\mathcal{G}_s^B = \left([E||3m] + [C_{2z}||(6mm - 3m)|3\tau] + [C_{2v}||\mathcal{P} \cdot 3m|4\tau] + [C_{2u}||\mathcal{P} \cdot (6mm - 3m)|\tau] \right).$$

The *broken helical* spin space group generators are given by the set of pairs $[C_{2z}||C_{6z}|3\tau]$, $[C_{2z}||m_v|3\tau]$, $[C_{2v}||\mathcal{P}|4\tau]$, and $[C_{2z}\mathcal{T}||\mathcal{T}]$.

Appendix C: Collinear phase of EuIn₂As₂

The collinear magnetic order of EuIn₂As₂ is described by the nontrivial spin Laue group $\mathbf{R}_S = [E||3m] + [C_2||6/mmm - 3m]$, indicating a bulk g-wave antiferromagnetic order that enables four spin un-polarized nodal planes. The opposite spin sub-lattices are connected by the spin symmetries $[C_2||m_v]$, $[C_2||m_{v'}]$, $[C_2||m_{v''}]$, and $[C_2||m_z]$. The electronic band structure along the path $L - \Gamma - m_z(L)$ shows quadratic spin splittings around Γ , as expected for an even magnetic order.

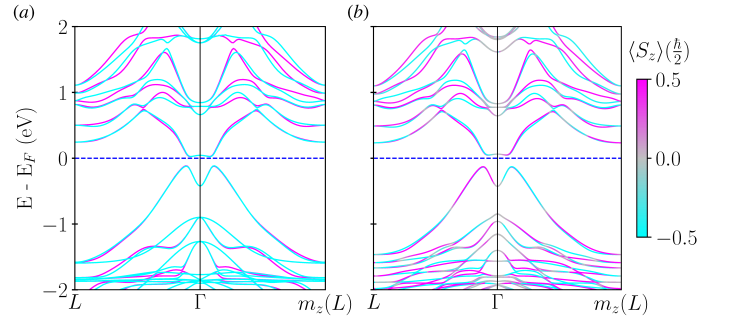


FIG. 6. Electronic band structure of the collinear EuIn₂As₂ order along $L - \Gamma - m_z(L)$ path, (a) without and (b) with spin-orbit coupling. The spin splittings are of non-relativistic origin, with values reaching up to 100 meV.

Appendix D: Linear Edelstein effect including spin-orbit coupling

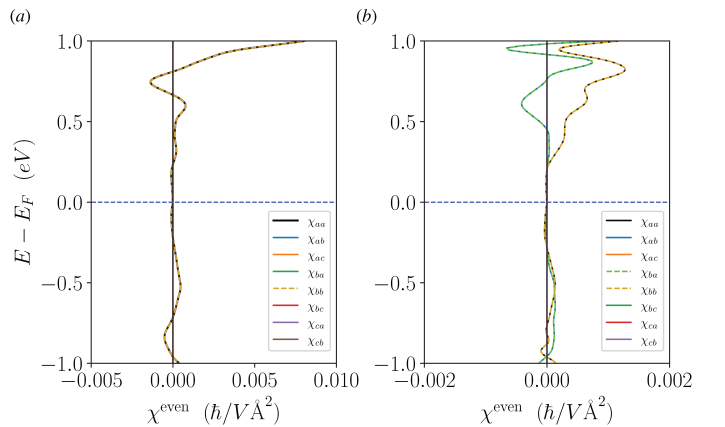


FIG. 7. **Intraband response tensor $\chi_{i,j}$ including spin-orbit coupling:** Calculations for the (a) helical and (b) broken-helical order with $\Gamma = 0.01$ eV. All out-of-plane components, except for χ_{cc} are zero, and the in-plane components adhere to the symmetry constraints outlined in Table I.

As previously discussed, without spin-orbit coupling, the only term that survives the spin symmetry constraints is

the out-of-plane Edelstein response χ_{cc} . When spin-orbit coupling is included, an in-plane response emerges for both the \mathcal{T} -even and \mathcal{T} -odd contributions. Figure 7 shows the intraband response $\chi_{i,j}$ with SOC for both the *helical*, and *broken-helical* order. We see that the in-plane response terms agree with the symmetry constraints listed in Table I and are approximately one order of magnitude smaller than the dominant non-relativistic χ_{zz} term.

Appendix E: Disorder-independent ratio

The intraband spin density scales with disorder scattering as $1/\Gamma$. To isolate the effects of the disorder, we compute the ratio between the intraband response tensor χ_{zz}^{even} and the longitudinal conductivity S_{zz} defined in Eq. E1. In Fig. 8(a), we show the longitudinal conductivity S_{zz} , featuring values within the typical range of conductivities observed in semiconductors. Finally, in Fig 8(b) we plot the disorder-independent ratio, which highlights a clear distinction between both phases, with values in the *helical* phase four times larger than those in the *broken helical* phase.

$$S_{ij} = \frac{e^2}{\Gamma\hbar} \int \frac{d^3\vec{k}}{(2\pi)^3} \sum_n \text{Re}[(\hat{v}_i)_{nn}(\hat{v}_j)_{nn}] \times \delta(E_{\vec{k}n} - E_F), \quad (\text{E1})$$

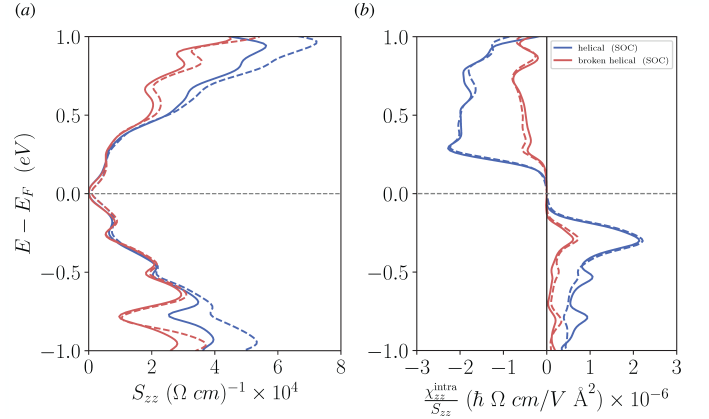


FIG. 8. **Longitudinal conductivity and disorder-independent spin density:** (a) The longitudinal S_{zz} conductivity in the *helical* (red solid line) and *broken helical* (blue solid line) phases. The dashed lines correspond to calculations without SOC. (b) The ratio between the intraband spin density and the longitudinal conductivity, resulting in a disorder independent quantity.

-
- [1] H. Li, S.-Y. Gao, S.-F. Duan, Y.-F. Xu, K.-J. Zhu, S.-J. Tian, J.-C. Gao, W.-H. Fan, Z.-C. Rao, J.-R. Huang, *et al.*, Dirac surface states in intrinsic magnetic topological insulators EuSn_2As_2 and $\text{MnBi}_{2n}\text{Te}_{3n+1}$, *Physical Review X* **9**, 041039 (2019).
- [2] T. Sato, Z. Wang, D. Takane, S. Souma, C. Cui, Y. Li, K. Nakayama, T. Kawakami, Y. Kubota, C. Cacho, *et al.*, Signature of band inversion in the antiferromagnetic phase of axion insulator candidate EuIn_2As_2 , *Physical Review Research* **2**, 033342 (2020).
- [3] G. M. Pierantozzi, A. De Vita, C. Bigi, X. Gui, H.-J. Tien, D. Mondal, F. Mazzola, J. Fujii, I. Vobornik, G. Vinai, *et al.*, Evidence of magnetism-induced topological protection in the axion insulator candidate EuSn_2P_2 , *Proceedings of the National Academy of Sciences* **119**, e2116575119 (2022).
- [4] N. A. Á. Pari, V. K. Bharadwaj, R. Jaeschke-Ubiergo, A. Valadkhani, R. Valentí, L. Šmejkal, and J. Sinova, Strain control of band topology and surface states in antiferromagnetic EuCd_2As_2 , *Physical Review B* **109**, 195117 (2024).
- [5] P. Rosa, Y. Xu, M. Rahn, J. Souza, S. Kushwaha, L. Veiga, A. Bombardi, S. Thomas, M. Janoschek, E. Bauer, *et al.*, Colossal magnetoresistance in a nonsymmorphic antiferromagnetic insulator, *npj Quantum Materials* **5**, 52 (2020).
- [6] S. Krebber, M. Kopp, C. Garg, K. Kummer, J. Sichelschmidt, S. Schulz, G. Poelchen, M. Mende, A. V. Virovets, K. Warawa, *et al.*, Colossal magnetoresistance in EuZn_2P_2 and its electronic and magnetic structure, *Physical Review B* **108**, 045116 (2023).
- [7] S. Luo, Y. Xu, F. Du, L. Yang, Y. Chen, C. Cao, Y. Song, and H. Yuan, Colossal magnetoresistance and topological phase transition in EuZn_2As_2 , *Physical Review B* **108**, 205140 (2023).
- [8] Y. Xu, Z. Song, Z. Wang, H. Weng, and X. Dai, Higher-order topology of the axion insulator EuIn_2As_2 , *Physical review letters* **122**, 256402 (2019).
- [9] J. Ma, H. Wang, S. Nie, C. Yi, Y. Xu, H. Li, J. Jandke, W. Wulfhekel, Y. Huang, D. West, *et al.*, Emergence of nontrivial low-energy dirac fermions in antiferromagnetic EuCd_2As_2 , *Advanced Materials* **32**, 1907565 (2020).
- [10] Y. Zhang, K. Deng, X. Zhang, M. Wang, Y. Wang, C. Liu, J.-W. Mei, S. Kumar, E. F. Schwier, K. Shimada, *et al.*, In-plane antiferromagnetic moments and magnetic polaron in the axion topological insulator candidate EuIn_2As_2 , *Physical Review B* **101**, 205126 (2020).
- [11] S. X. Riberolles, T. V. Trevisan, B. Kuthanazhi, T. Heitmann, F. Ye, D. Johnston, S. Bud'ko, D. Ryan, P. Canfield, A. Kreyssig, *et al.*, Magnetic crystalline-symmetry-protected axion electrodynamics and field-tunable unpinned dirac cones in EuIn_2As_2 , *Nature communications* **12**, 999 (2021).
- [12] J.-R. Soh, A. Bombardi, F. Mila, M. C. Rahn, D. Prabhakaran, S. Francoual, H. M. Rønnow, and A. T. Boothroyd, Understanding unconventional magnetic order in a candidate axion insulator by resonant elastic x-ray scattering, *Nature Communications* **14**, 3387 (2023).
- [13] E. Donoway, T. Trevisan, A. Liebman-Peláez, R. Day, K. Yamakawa, Y. Sun, J. Soh, D. Prabhakaran, A. Boothroyd, R. Fernandes, *et al.*, Multimodal approach reveals the symmetry-breaking pathway to the broken helix in EuIn_2As_2 , *Physical Review X* **14**, 031013 (2024).
- [14] H. Takeda, J. Yan, Z. Jiang, X. Luo, Y. Sun, and M. Yamashita, Incommensurate magnetic order in an

- axion insulator candidate EuIn_2As_2 investigated by nmr measurement, *npj Quantum Materials* **9**, 67 (2024).
- [15] M. Gen, Y. Fujishiro, K. Okigami, S. Hayami, K. Adachi, D. Hashizume, T. Kurumaji, H. Sagayama, H. Nakao, Y. Tokura, *et al.*, Incommensurate broken-helix and broken-fanlike states in axion insulator candidate EuIn_2As_2 , arXiv preprint arXiv:2403.03022 (2024).
- [16] G. Cuono, R. M. Sattigeri, C. Autieri, and T. Dietl, Ab initio overestimation of the topological region in eu-based compounds, *Physical Review B* **108**, 075150 (2023).
- [17] D. B. Litvin and W. Opechowski, Spin groups, *Physica* **76**, 538 (1974).
- [18] D. B. Litvin, Spin point groups, *Acta Crystallographica Section A: Crystal Physics, Diffraction, Theoretical and General Crystallography* **33**, 279 (1977).
- [19] A. B. Hellenes, T. Jungwirth, J. Sinova, and L. Šmejkal, Exchange spin-orbit coupling and unconventional p-wave magnetism, arXiv preprint arXiv:2309.01607 (2023).
- [20] L. Šmejkal, J. Sinova, and T. Jungwirth, Emerging research landscape of altermagnetism, *Physical Review X* **12**, 040501 (2022).
- [21] A. Manchon, J. Železný, I. M. Miron, T. Jungwirth, J. Sinova, A. Thiaville, K. Garello, and P. Gambardella, Current-induced spin-orbit torques in ferromagnetic and antiferromagnetic systems, *Reviews of Modern Physics* **91**, 035004 (2019).
- [22] G. Bihlmayer, P. Noël, D. V. Vyalikh, E. V. Chulkov, and A. Manchon, Rashba-like physics in condensed matter, *Nature Reviews Physics* **4**, 642 (2022).
- [23] J. Železný, H. Gao, K. Vybourný, J. Zemen, J. Mašek, A. Manchon, J. Wunderlich, J. Sinova, and T. Jungwirth, Relativistic néel-order fields induced by electrical current in antiferromagnets, *Physical review letters* **113**, 157201 (2014).
- [24] R. González-Hernández, P. Ritzinger, K. Vybourný, J. Železný, and A. Manchon, Non-relativistic torque and edelstein effect in non-collinear magnets, *Nature Communications* **15**, 1 (2024).
- [25] A. Chakraborty, A. B. Hellenes, R. Jaeschke-Ubierno, T. Jungwirth, L. Šmejkal, and J. Sinova, Highly efficient non-relativistic edelstein effect in p-wave magnets, arXiv preprint arXiv:2411.16378 (2024).
- [26] I. Garate and A. H. MacDonald, Influence of a transport current on magnetic anisotropy in gyrotropic ferromagnets, *Physical Review B—Condensed Matter and Materials Physics* **80**, 134403 (2009).
- [27] H. Li, H. Gao, L. P. Zârbo, K. Vybourný, X. Wang, I. Garate, F. Doğan, A. Čejchan, J. Sinova, T. Jungwirth, *et al.*, Intraband and interband spin-orbit torques in noncentrosymmetric ferromagnets, *Physical Review B* **91**, 134402 (2015).
- [28] J. Yan, J. Si, Z. Jiang, H. Ma, Y. Uwatoko, B.-T. Wang, X. Luo, Y. Sun, and M. Yamashita, Doping-tunable fermi surface with persistent topological hall effect in the axion candidate EuIn_2As_2 , *Physical Review B* **110**, 115111 (2024).
- [29] G. Kresse and J. Furthmüller, Efficient iterative schemes for ab initio total-energy calculations using a plane-wave basis set, *Physical review B* **54**, 11169 (1996).
- [30] G. Kresse and D. Joubert, From ultrasoft pseudopotentials to the projector augmented-wave method, *Physical review b* **59**, 1758 (1999).
- [31] J. P. Perdew, K. Burke, and M. Ernzerhof, Generalized gradient approximation made simple, *Physical review letters* **77**, 3865 (1996).
- [32] S. V. Gallego, J. M. Perez-Mato, L. Elcoro, E. S. Tasci, R. M. Hanson, K. Momma, M. I. Aroyo, and G. Madariaga, Magndata: towards a database of magnetic structures. i. the commensurate case, *Journal of Applied Crystallography* **49**, 1750 (2016).
- [33] Labels of the non-collinear magnetic phases of EuIn_2As_2 in magndata: helical(#1.0.31), broken-helical(#1.0.32), .
- [34] P.-W. Ma and S. Dudarev, Constrained density functional for noncollinear magnetism, *Physical Review B* **91**, 054420 (2015).
- [35] U. Herath, P. Tavadze, X. He, E. Bousquet, S. Singh, F. Muñoz, and A. H. Romero, Pyprocar: A python library for electronic structure pre/post-processing, *Computer Physics Communications* **251**, 107080 (2020).
- [36] K. Shinohara, A. Togo, H. Watanabe, T. Nomoto, I. Tanaka, and R. Arita, Algorithm for spin symmetry operation search, *Acta Crystallographica Section A: Foundations and Advances* **80** (2024).
- [37] G. Pizzi, V. Vitale, R. Arita, S. Blügel, F. Freimuth, G. Géranton, M. Gibertini, D. Gresch, C. Johnson, T. Koretsune, *et al.*, Wannier90 as a community code: new features and applications, *Journal of Physics: Condensed Matter* **32**, 165902 (2020).
- [38] S. S. Tsirkin, High performance wannier interpolation of berry curvature and related quantities with wannierberri code, *npj Computational Materials* **7**, 33 (2021).